Journal of Materials Research and Technology 42 (2026) 10851–10863

Contents lists available at ScienceDirect

Journal of Materials Research and Technology

journal homepage: www.elsevier.com/locate/jmrt

In-situ process monitoring and control of laser directed energy deposition using thermal imaging and computer vision

Saegis Abbott [a,b,1], Kassandra Hernandez [a,b,1], Ryan Bertelsen [a,b], Omid Hatami Farzaneh [a,b], Adam Bischoff [a], Doug Dingus [b,c], Dong Lin [a,b], Jesse Rodriguez [a,b,*], Devin J. Roach [a,b,**]

[a] School of Mechanical, Industrial, and Manufacturing Engineering, Oregon State University, Corvallis, OR, 97331, USA
[b] Advanced Technology and Manufacturing Institute (ATAMI), Corvallis, OR, 97330, USA
[c] On Additive, 16066 Boones Ferry Rd, Suite F, Tigard, OR, 97223, USA

ARTICLE INFO

Keywords:
3D printing
Direct energy deposition
Infrared imaging
Metals
Microstructure control
Real time optimization

ABSTRACT

Laser direct energy deposition (LDED) is a prominent additive manufacturing (AM) technique due to its high deposition rates, scalability, and material efficiency. However, maintaining consistent part quality remains a significant challenge due to complex thermal cycles inherent to high-deposition processes, where rapid heat accumulation and varying cooling rates lead to heterogeneous microstructures and residual stress. This work introduces a data-driven in-situ process monitoring and control (ISPMC) framework for wire-fed LDED that combines high-speed infrared (IR) tomography, computer vision, and real-time process parameter adjustment to improve print quality. Here, high-speed infrared (IR) thermography was used to capture optical heat mapping and temperature history data, providing real-time insights into heat transfer and microstructural evolution. By integrating the IR data with computer vision, a predictive framework was developed for real-time adaptive control of LDED process parameters. Experimental validation demonstrated significant improvements in thermal stability, visual quality, and microstructural homogeneity across complex geometries. Optical microscopy revealed that No ISPMC samples developed dendritic and cellular grain structures, whereas ISPMC samples produced consistent equiaxed cellular grains throughout the build. Mechanical testing showed up to a 90% reduction in ductility variance and a 49% reduction in ultimate tensile strength variance compared to the No ISPMC samples. Nano-indentation further confirmed reduced hardness and modulus gradients throughout the build height, demonstrating improved thermal and mechanical homogeneity. These results establish ISPMC as an effective closed-loop control framework for reliable production of high-quality metal AM components.

1. Introduction

Metal additive manufacturing (MAM) is currently revolutionizing manufacturing, engineering, and design by enabling on-demand fabrication and repair of production parts ranging from appliances to aerospace components [1–5]. Since MAM provides a straightforward approach for fabricating widely customizable part geometries, it is uniquely capable of generating a paradigm shift in metal component prototyping and the fabrication of large-scale parts. Furthermore, researchers have developed novel materials compatible with many new processes utilizing laser melting techniques with specialty metal powders rather than binders and ex-situ sintering [6,7]. Laser powder bed fusion (LPBF) is one of the most well-known MAM approaches, as it is a promising technology that selectively melts powder into a given shape layer by layer to create geometrically complex 3D components [8–15]. Despite its advantages, LPBF components are highly restricted by small build volumes, slow processing time, and porosity due to keyholing of the laser weld, restricting their application to select industrial applications [16,17]. Another promising MAM approach is laser direct energy deposition (LDED), which utilizes confocal lasers to irradiate and fuse a single flow of powder or wire-based metals to a given substrate 9,10,18. LDED has recently seen growth due to its potential for multi-material part fabrication [19,20]. Powder LDED allows for larger print sizes and faster deposition than LPBF; yet it struggles with powder overshoot,

* Corresponding author. 236 Rogers Hall, Corvallis, OR, 97331, USA.
** Corresponding author. 236 Rogers Hall, Corvallis, OR, 97331, USA.
E-mail addresses: jesse.rodriguez@oregonstate.edu (J. Rodriguez), devin.roach@oregonstate.edu (D.J. Roach).
[1] co-first author.

https://doi.org/10.1016/j.jmrt.2026.05.322
Received 11 April 2026; Received in revised form 18 May 2026; Accepted 25 May 2026
Available online 28 May 2026

where voids are filled with unmelted powder, resulting in substantial costs due to material waste, especially when using specialty materials. These parts also tend to have higher porosity rates in the prints, which reduce component strength and thermal conductivity, significantly limiting the application space for powder LDED [21].

To address these limitations, recent efforts have focused on MAM using welding wires, making wire-based LDED more accessible and resulting in a broader selection of materials for printing applications [22,23]. By utilizing a wire feed rather than metal powders, LDED has demonstrated high deposition rates and increased part density, enabling fabrication of large parts and high production volumes at lower material costs [24–29]. With optimized process parameters, LDED also enables printing of hollow geometries with no filler or support material, a characteristic unique to LDED [30,31]. Nonetheless, wire-based LDED exhibits key challenges that need to be overcome before it can be utilized in production systems. Most notably, high defect rates stemming from trial-and-error-based process parameter optimization lead to significant post-processing or scrapping of parts, reducing the material savings from using additive manufacturing (AM) compared to subtractive manufacturing. Variable part microstructures are another challenge that can lead to premature part failure and reduced mechanical properties, like strength and ductility [29,32–34]. These challenges commonly manifest as excessive surface roughness, porosity, cracking, geometric distortion, residual stress accumulation, and inconsistent microstructures throughout the build. These issues become particularly severe in large or thin-walled geometries, where heat accumulation and unstable thermal cycling are more significant [35–37]. Such defects often reduce dimensional accuracy, mechanical reliability, and overall component performance, limiting the direct use of as printed LDED parts in critical applications. Research has attempted to address these issues through post-processing methods such as machining, heat treatment, hot isostatic pressing (HIP), and surface finishing to reduce residual stress, improve dimensional accuracy, and enhance the resulting mechanical properties of LDED components [38,39]. While these approaches can improve final part quality, they are typically costly, time intensive, and performed only after defects and thermal inconsistencies have already formed during deposition. As a result, there remains a critical need for real-time process monitoring and control strategies capable of mitigating these defects during fabrication rather than correcting them in post processing.

Ex-situ methods have been utilized to analyze LDED-printed components, characterizing the resulting quality and microstructure using a range of advanced techniques [40]. Tensile testing provides a quantitative measure of mechanical properties, including yield strength, ultimate tensile strength, and ductility, revealing how print parameters influence macroscopic performance [41,42]. However, this technique does not reveal the microstructural elements of grain size and structure. Optical imaging microscopy, with chemical etching, allows for initial assessment of bead uniformity. It reveals visible defects such as large pores, and layer adhesion, as well as grain size and structure across the parts [43,44]; although it still does not determine the mechanical properties of the metal, such as modulus and strength. X-ray Diffraction (XRD) identifies crystallographic phases, measures residual stresses, and assesses part texture [45]. However, it cannot be performed in situ, with the sample either being surface tested, or often being destroyed and reduced to a powder in order to determine crystal structure. Microhardness and nanoindentation testing offer localized measurements of the material properties specifically focused on hardness and elastic-plastic response, enabling correlation between microstructural features and small-scale mechanical behavior, with nanoindentation allowing for grain-specific measurements [46,47]. Scanning Electron Microscopy (SEM) provides higher-resolution imaging of surface morphology, defect distributions, and microstructural features such as dendritic structures or precipitates [48,49]. Transmission Electron Microscopy (TEM) enables nanoscale analysis of dislocations, sub-grain structures, and fine precipitates that form during rapid solidification [48,50]. Electron Backscatter Diffraction (EBSD) is used to map grain orientation, quantify grain size and texture, and identify phase boundaries or misorientation features [51,52]. Together, these techniques quantify porosity, grain structures, and mechanical properties, providing critical insights into the interactions among print parameters, material behavior, and evolving microstructure [53]. Nonetheless, these approaches are all ex-situ, still requiring re-printing to address any of the issues, significantly delaying the iteration process for both the LDED technology and the desired printed component.

Researchers have integrated some of these techniques into advanced MAM platforms to learn more about intricate physics throughout the printing process, termed in-situ process monitoring 54–56. Gould et al. successfully integrated in-situ X-ray imaging and diffraction to monitor the melt pool in LPBF and discovered that the combined data could correlate defects to melt pool conditions as well as identify residual stresses in the part [57,58]. Other researchers have implemented similar monitoring techniques into well-understood AM processes like FDM and LPBF, allowing for real-time defect detection and quantification [59–61]. Nonetheless, in-situ process monitoring alone cannot correct the detected defects. Some open-loop process control has been implemented for MAM to attempt to address identified defects, and has reduced the failure rate of some prints [62]. Unfortunately, this still falls short of eliminating the tedious trial-and-error process, which is still required to correct errors detected in situ.

To truly take full advantage of in-situ monitoring capabilities, some researchers have proposed using a real-time closed-loop method of process control based on in-situ data collection [29,63]. Real-time monitoring for parameter adjustments has been successfully implemented with real-time computer vision systems and artificial intelligence for optimization and analysis of 3D printed foams [64]. Further research in polymers used a visual camera with a continuous stream of image data to feed computer vision and an invertible neural network (INN), creating a system that evaluates prints and then adjusts print parameters in real-time for closed-loop control [65]. Hernandez et al. further demonstrated the applicability of machine learning for predicting and optimizing mechanical behavior in AM polymer systems, highlighting the growing role of AI-driven approaches for improving AM process understanding and performance [66]. Algorithms have also been used to optimize the structural design of composites [67]. High-speed digital image correlation (DIC) has been developed to allow for 2D visual images to be processed to analyze a 3D space [68]. Further, Landauer et al. found that incorporating energy- and entropy-based q-factor metrics into DIC significantly improves the accuracy of evaluating displacement, reduces noise, and limits decorrelation under large image distortions [69]. However, complex material properties such as microstructure, mechanical strength, and part density, which continue to be major issues facing MAM, cannot be addressed using visual camera monitoring and control methods like those successfully implemented for polymer AM due to the complexity of the thermal physics and melt pool dynamics of MAM [70].

Infrared (IR)-based camera monitoring has proven highly effective in tracking the complex thermal physics of melt pool dynamics for polymers [71] and other MAM technologies, with Wang et al. discovering its applicability for tracking melt pool shape and keyholing, informing both the microstructure and the resulting properties of the parts [72–76]. Marshal et al. conducted research based on random print parameters while gathering the residual temperature history and the melt pool temperatures to quantify overheating and estimate the resulting microstructures [77]. Ya et al. showed that IR intensity signals could indicate the bonding state of metals in laser metal deposition, used for metal cladding of parts [78]. Ye et al. calls for further closed-loop process monitoring in LDED, and Herzog et al. demonstrate the feasibility of implementing effective IR monitoring, detecting the formation of structural features and defects like undesired filleting on corners [79]. Finally, Wei et al. demonstrated the use of an IR camera monitoring combined with a convolutional neural network (CNN) for real-time

microscopic defect detection in LPBF [80], which may be a promising approach for other MAM technologies, although it requires almost 10, 000 training images. Therefore, real-time, closed-loop control of part quality and microstructure of LDED printed components remains a key research challenge, requiring a combination of real-time process monitoring and physics-informed parameter adjustments.

This work presents an in-situ process monitoring and control (ISPMC) approach for wire LDED that combines IR-based in-situ monitoring to obtain melt-pool data with real-time computer vision analysis to suggest parameter changes based on melt-pool dynamics. Here, computer vision was used to quantify melt pool morphology and predict potential defects and microstructural variation. By suggesting real-time corrective actions based on analysis of the melt pool intensity, area, and glare in each IR image, the ISPMC approach can correct for potential errors before they occur. This real-time process control system was tested on a series of MAM prints with various complex part geometries, such as thin-wall shapes and geometric transitions. ISPMC enables real-time detection and mitigation of several common defects, including lack of adhesion and melt-pool collapse resulting from undermelting and overmelting, respectively. The ISPMC system adjusted various print parameters to effectively mitigate microstructure and quality issues, ultimately increasing quality, material properties, and microstructural consistency across the parts, paving the way for large-scale LDED production of quality parts with tailored microstructures and properties.

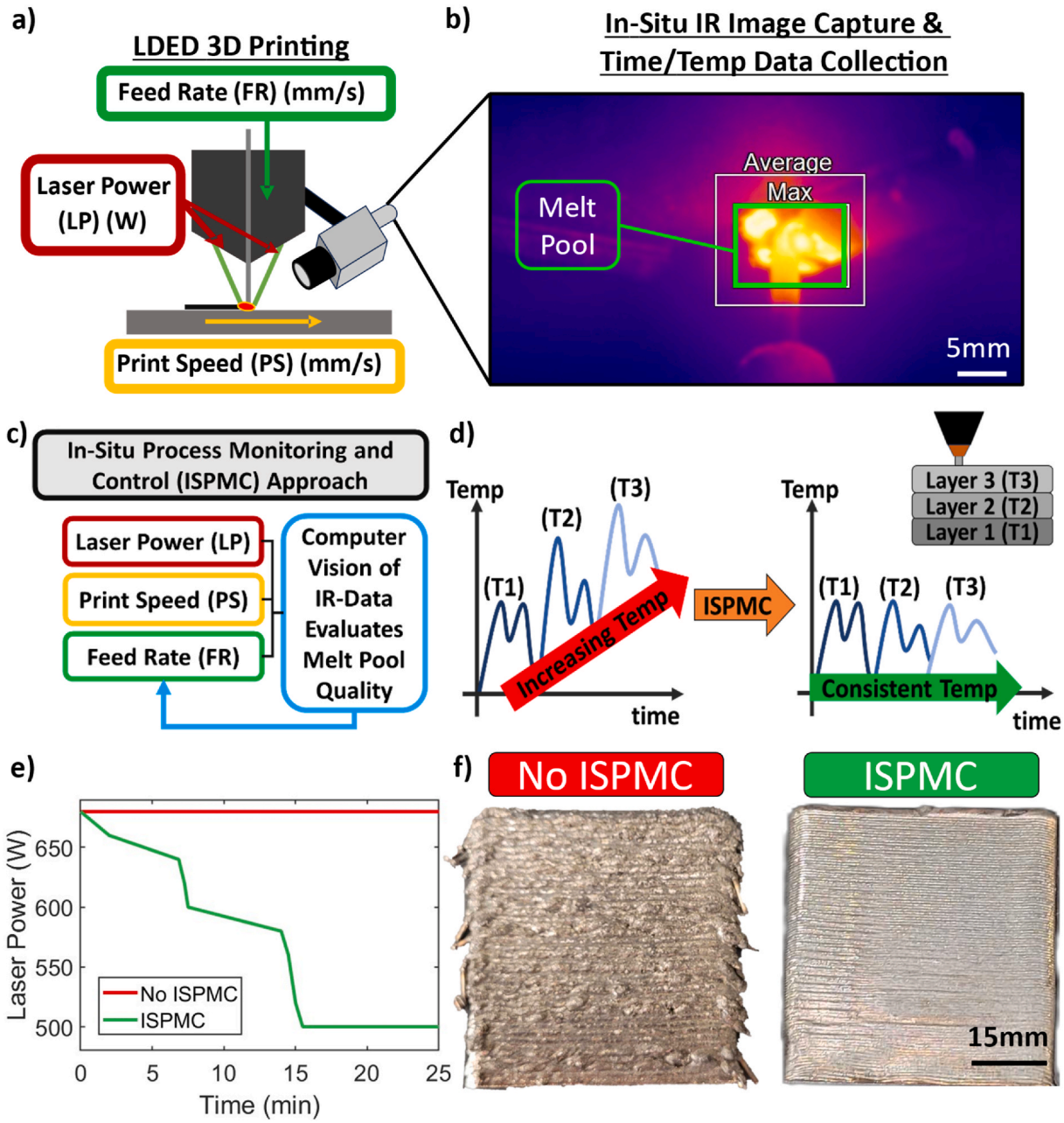

Fig. 1. In-situ Process Monitoring and Control (ISPMC) approach for LDED 3D printing. **a)** LDED 3D printing showing the primary process parameters of Laser Power, Feed Rate, and Print Speed. **b)** In-situ IR images capturing melt pool dynamics. **c)** ISPMC approach with computer vision providing feedback on print parameters. **d)** Temperature increases over time with unregulated prints, where ISPMC stabilizes melt pool temperatures using real-time adjustment of print parameters. **e)** ISPMC varied process parameters for laser power over time for thin-willed component. **f)** Visual improvements of the print quality through ISPMC optimization.

2. Results and discussion

2.1. Real-time data capture from LDED printing

To ensure consistent part quality and cohesive properties throughout a printed part, real-time monitoring is necessary during the LDED process. Here, real-time process monitoring of the key LDED process parameters, shown in Fig. 1a, was implemented by capturing images using a high-speed IR camera. The resulting IR images, as seen in Fig. 1b, allow a computer vision algorithm to track the melt pool dynamics. The computer vision algorithm could predict potential failures of the part as it analyzed the data faster than the capture rate, allowing for minimal latency in the real-time parameter corrections. Further details about the computer vision algorithm are described below in Section 3.2. Using the outputs from the computer vision algorithm, dynamic process control could be implemented to quickly adjust key LDED print parameters to achieve target properties. Using this, we developed an approach for performing in-situ process monitoring and control (ISPMC) of LDED, as outlined in Fig. 1c. Traditional, unregulated LDED prints result in increasingly higher melt pool temperatures during printing; however, ISPMC is capable of stabilizing the melt pool temperature throughout a print by modulating print parameters, as shown schematically in Fig. 1d. Fig. 1e shows an example where the most critical process parameter, laser power, was adjusted to address temperature leading to over-melting and under-melting. The other process parameters, print speed and feed rate, are less ideal for initial corrections due to the proportionality requirements to maintain a constant rate of material deposition. These challenges become particularly clear when fabricating complex geometries and thin-walled structures, which necessitate modifications of all three primary parameters, as will be shown later in this study.

Thin-walled structures have long been a challenge for MAM, as the heat capacity is small and there is ample opportunity for asymmetric melting and drooping. During wire LDED printing of thin-wall geometries, maintaining consistent contact between the wire and substrate is a challenge, as the wire can deflect away from the melt pool. This limits the build quality of parts, especially at higher deposition speeds. This issue is predominant in fins and other thin-walled features, which are common geometries in aerospace components where aerodynamics and thermal management are critical properties. The different geometries tested included fins, cones, and geometric transitions, which showed that ISPMC is capable of improving quality in thin-walled parts, as seen in Fig. 1f. The Z pattern shown on the fin parts is the result of start-stop locations for each layer, which had no known significant effect on the results of our experiments.

2.2. In-situ defect detection and real-time process control

A computer vision algorithm was developed that used the in-situ IR data to quantify melt pool intensity, edge-derived area, and glare. These factors were correlated with defect formation, allowing the expected process outcomes to be inferred for each melt pool condition. The images were processed by extracting the edge-based and intensity-based features. These features were subsequently used to compute a quality score, classify the melting state, and recommend a corrective process action. The images were first normalized using a min-max normalization to account for variations in absolute signal intensity across frames. These normalized images were converted to an 8-bit grayscale representation for image processing. To enhance spatial gradients associated with the melt pool boundaries, a Gaussian blur was applied to suppress high-frequency noise. Edge detection was then performed using Sobel operators in both the horizontal and vertical directions to produce an edge map, which was quantified as the edge area. The intensity was computed to capture overexposure and glare effects using pixels that exceeded 95% of the normalized intensity range. These metrics were used to impose penalties on the quality score and determine if the melt pool has an under- or over-melting state as described below in Fig. 2. A scalar quality score ranging from 1 to 10 was then assigned to each frame based on a weighted combination of edge area, intensity, and glare. Frames with low edge content and low intensity were automatically assigned the lowest quality score, corresponding to insufficient melting or a loss of the melt pool signal. The penalties were subtracted from the nominal maximum score to reflect increasing melt instability, glare, or saturation effects.

The physical interpretation of these conditions is illustrated below in Fig. 2. In an under-melting condition, the wire fails to melt and bends on the print surface, feeding out from the sides of the print, creating defects as shown in Fig. 2a. The overmelting condition occurs when the melt pool expands laterally over the sides of the part, resulting in surface roughness and layer failures, identified by high intensity and a long tail region shown in Fig. 2b. The optimal melt pool condition, as shown in Fig. 2c, occurs when the print has layers of consistent height being deposited at a constant rate with consistent melt pool and minimal trailing tail of melted metal. If resulting errors are identified, either under- or over-melting, then a variety of actions are considered by the ISPMC approach. With several parameters at its disposal, the program begins with the best-suited option and then fine-tunes with other options based on the system's response. In the under-melting case, the system will first increase the laser power. If the issues persist, it then reduces the print speed to allow for better absorption of the energy into the metal. For over-melting scenarios, the program will decrease the laser power first, then increase the print speed to help cool the part if geometry allows. The failure analysis, diagnosis, and suggested parameter corrections were performed via a Python code that uses computer vision to detect the failure cases. It then associates each case with the best action to take based on the duration and severity of the issue, while also considering previous corrections and past parameter combinations that were successful. This image processing and scoring framework provides a straightforward approach for real-time melt quality assessment and establishes a foundation for closed-loop control and data-driven modeling of the wire-LDED process.

2.3. Comparison of ISPMC and No ISPMC microstructure and properties

During printing, increased melt pool temperatures begin to anneal the initial layers of the part. If melt pool temperatures are left uncorrected, these annealing effects create larger grain structures that are more ductile in nature. To study this, stainless steel (SS316L) was selected due to its austenite-to-austenite transition during melting. This property minimizes microstructural variability in LDED and isolates the effect of ISPMC on the resulting grain structure. To study this, thin wall fins were printed, as seen in Fig. 3a, using both ISPMC and no ISMPC, where the process parameters were adjusted during the print. Optical Imaging Microscopy was used to view the resulting grain structures at both the top and bottom of the samples. The results, shown in Fig. 3b, found that the No ISPMC samples showed dendritic grains at the top of the part with more equiaxed cellular grains at the bottom. In contrast, ISPMC samples had consistent equiaxed cellular grains across the entire part. These results validate the expected effects of the thermal trends indicated by the IR data on the resulting grain structure. Overmelting, driven by high heat input, liquidizes the metal, which then rapidly cools, creating a more chaotic combination of columnar, cellular, and dendritic grains at the top of the part, while lower layers with lower heat input have columnar and cellular grains at the bottom. In contrast, the ISPMC samples with lower heat input have consistent cellular grain formation across the entire part [81–83]. An analysis of the print parameters reveals that constant laser power results in lower part quality due to an excess of thermal energy distributed throughout the print. In contrast, ISPMC decreases laser power, resulting in an optimal input of thermal energy throughout the print, as shown in Fig. 3c. This effect ultimately produces a softer microstructure in the lower layers across the part and a harder microstructure at the top. Due to the observed improvements to

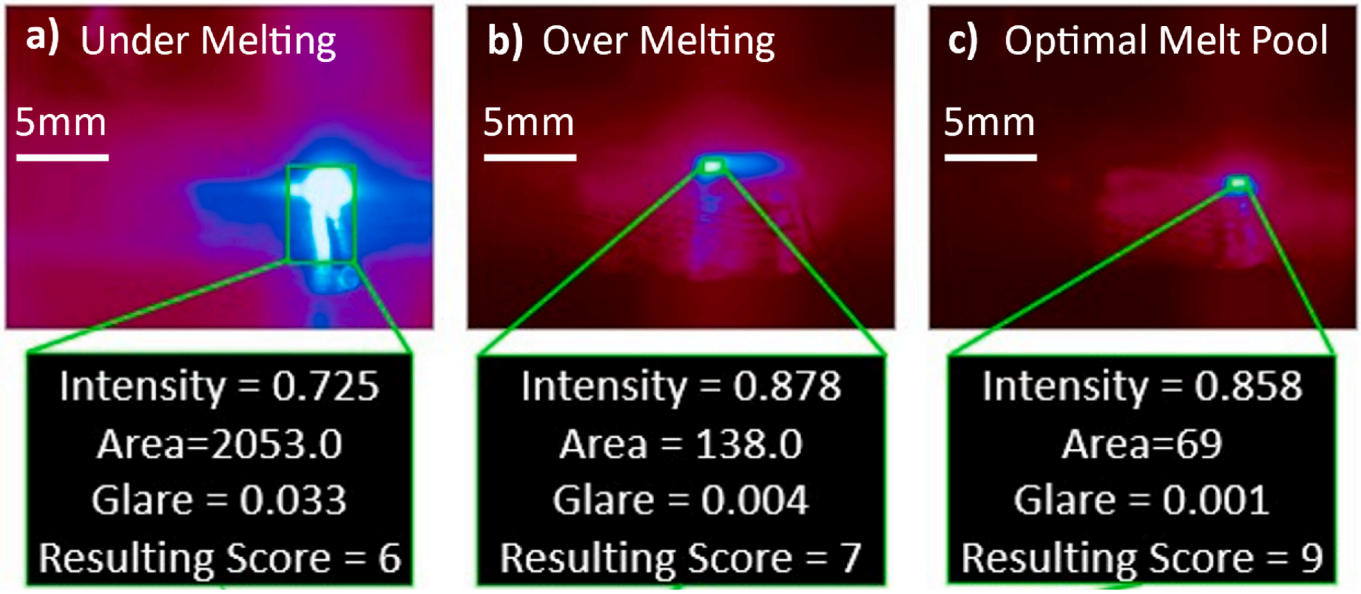

Fig. 2. Computer vision approach for melt pool analysis. **a)** The IR image shows high glare caused by laser reflection, and lower intensity with an extremely large area, leading to undermelting. **b)** Higher Intensity, with some glare and a large area identified as overmelting due to the melt pool also having a large trailing melted section. **c)** optimal melt pool with good intensity, small glare, and small area (less than 100).

microstructure for annealed regions in the prints, post-process annealing could be an effective strategy for improving part microstructure and properties. To determine these microstructural trends on the overall material properties, mechanical testing was performed at various locations on a single part. As shown in Fig. 3d, the results show high variance in material strength and ductility for No ISPMC samples and low variance in ISPMC samples. For the No ISPMC sample shown, it was observed that the lower layers with annealed microstructure have wide variability in ductility and ultimate tensile strength. The ISPMC sample, however, showed consistency in both ductility and ultimate tensile strength, with up to 91% reduction in ductility variance from a strain variance of 0.31 to 0.003 and 49% reduction in ultimate tensile strength variance from a stress variance of 56.1 MPa to 28.4 MPa, as shown in Table S1. This variance decrease was a direct result of the quantity and rate of parameter variations driven by the ISPMC approach.

2.4. Real-time correction and resulting mechanical properties

Process parameters drive the resulting quality and properties of 3D printed parts. Therefore, process parameters from iterative ISPMC optimization trials were analyzed and plotted in Fig. 4a–aid in the refinement and analytical understanding of ISPMC. These results reveal a clear optimal zone for laser power levels, as both too rapid and too slow power corrections resulted in greater materials property variance. This was revealed by tensile testing of samples cut from the bottom, middle, and top of 3D printed fins. The results shown in Fig. 4b show a continued progression of in-situ monitoring, informed parameter adjustments further tailored each generation to find the optimal frequency and increment of change to the laser power throughout the parts. Starting with the first part that had No ISPMC, it was clear that the power levels were too high, leading to overmelting conditions. This led to ISPMC 01 and 02 having large corrections in power levels, reducing them to 300 W and 400 W, respectively. However, it was found that operating below 500 W resulted in undermelting conditions for these parts. As such, subsequent trials were conducted at or above laser power levels of 500 W. ISPMC 03 saw a successful print, but it still did not correct the overmelting conditions soon enough to fully mitigate the resulting property variance. ISPMC04 improved upon this by decreasing power levels more rapidly, which resulted in some undermelting due to the rapid decrease in power. This was addressed in ISPMC05, which had a slightly lighter decrease in power initially compared to ISPMC04. Unfortunately, this trial still saw more variance than desired. ISPMC06 addressed the former issues by having significant decreases in laser power and then maintaining that power level for some time to reduce both undermelting and overmelting conditions. This approach was successful, although it resulted in the middle layers being overannealed and having significantly higher ductility than the top and bottom layers. To address this, the final power decrease to 500 W was implemented earlier for ISPMC07, as shown in Fig. 4a, resulting in over 90% reduction in ductility variance compared to the ISPMC sample and 49% reduction in ultimate tensile strength variance.

These tests revealed that each generation of the ISPMC samples achieved improved mechanical property consistency compared to the No ISPMC sample. To study the aggregate effect on parts, total energy entering the print for each generation was plotted against the ductility variance for each sample, as seen in Fig. 4c. The resulting plot shows a clear trend where non-optimized total energy input results in greater property variance. It was seen that No ISPMC sample had a brittle structure at the top and a more ductile structure on the bottom, resulting in higher strengths at the lower layers. This is from subsequent layer annealing, which is a side effect of an overheated melt pool. The first layers on the bottom of each print initially become hard due to the cold temperature of the printing surface. As time goes on, additional heat flows through the lower layers, the Austenite grains continue to grow, and the properties become increasingly ductile. Later print layers tend to be more ductile initially due to the increased residual heat on the surface, but do not have as much heat conducted through them to the build plate and thus are not annealed as highly as the layers on the bottom. A plot of the power vs time for ISPMC 03, ISPMC05, and ISPMC07 is provided in Fig. S1a of the SI for closer comparison of those trials. Additionally, total energy vs ultimate tensile strength is also included in the SI as Fig. S1b. Since the ISPMC05 bottom sample slipped while being tensile tested, it was removed when considering the variance of this sample.

To extend the analysis beyond the variance identified through tensile testing, nano-indentation was used to quantify grain-scale hardness and modulus for samples printed with both No ISPMC and ISPMC. Measurements were taken at the top and bottom of the samples in the lo-

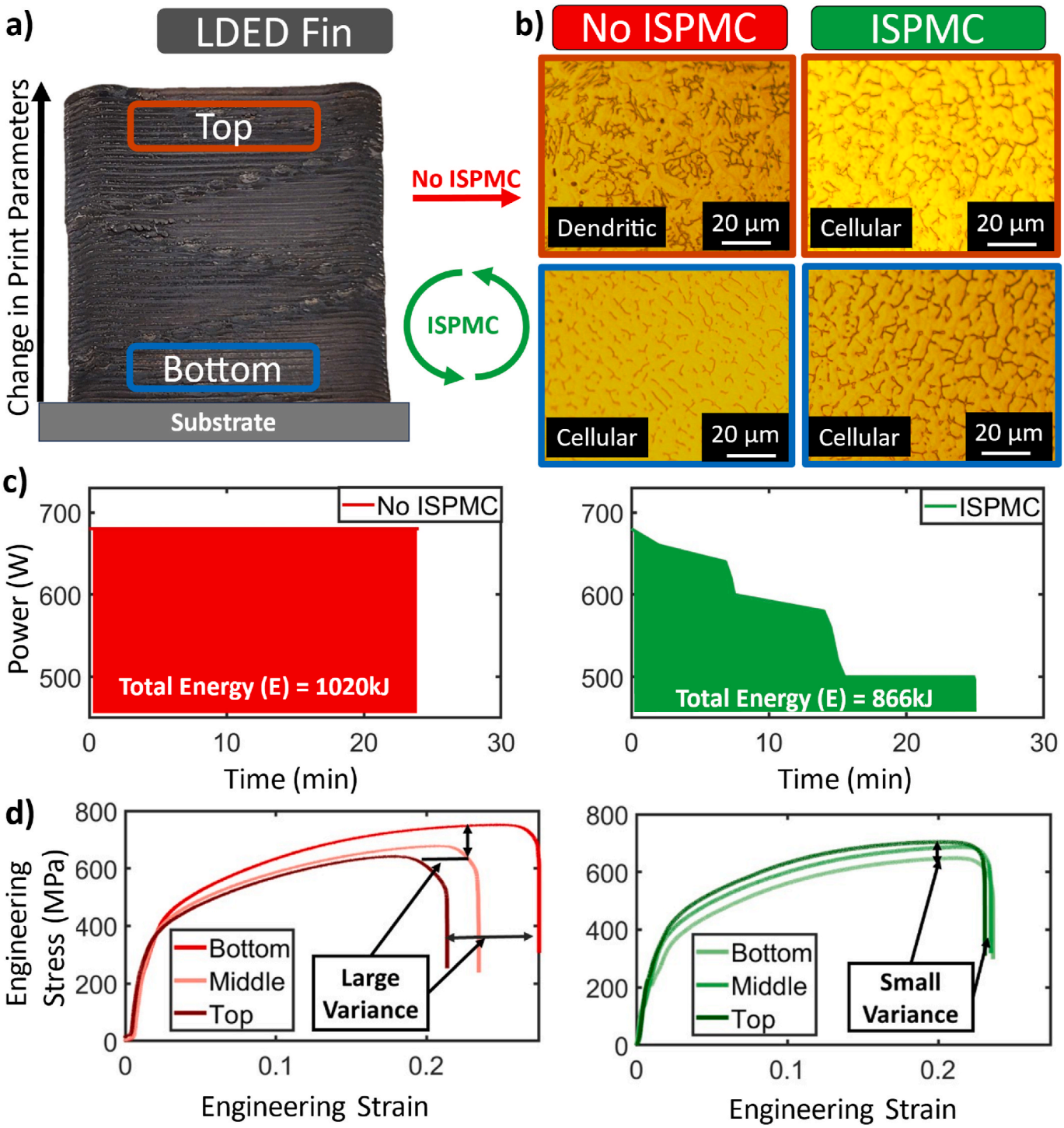

Fig. 3. Comparison of No ISPMC vs ISPMC microstructure and resulting properties. **a)** LDED printed fin with No ISPMC vs with ISPMC comparison of print parameters change with relation to build direction. **b)** Comparison of microstructure characteristics from the top (dark orange) and bottom (blue). **c)** Depicts the change in printing parameters and total thermal energy passing through No ISPMC and ISPMC prints, respectively. **d)** Tensile testing reveals high material property variance in No ISPMC samples and consistent material properties in ISPMC samples.

cations indicated in Fig. 5a and b where the fins were cut to reveal the interior surface to perform nano-indentation. The results of the No ISPMC sample, shown in Fig. 5c, reveal that the hardness at the top of the fin was generally much lower compared to the ISPMC sample hardness shown in Fig. 5d, indicating a lower local strength in this area compared to the bottom region of the build. Due to inherent variability in hardness measurements, a statistical comparison between the top and bottom regions of the build was performed. The No ISPMC sample exhibited a larger difference between the top and bottom at 0.39 GPa compared to the ISPMC sample at 0.15 GPa. A two-way ANOVA revealed a statistically significant interaction between sample and region given a p value of $5.68x10^{-24}$ indicating that the effect of location on hardness depends on the processing conditions. This comparison further confirms that the No ISPMC sample produces a stronger differentiation in hardness between deposition layers, whereas the ISPMC sample results in a more uniform hardness distribution. The boxplot results of the ANOVA

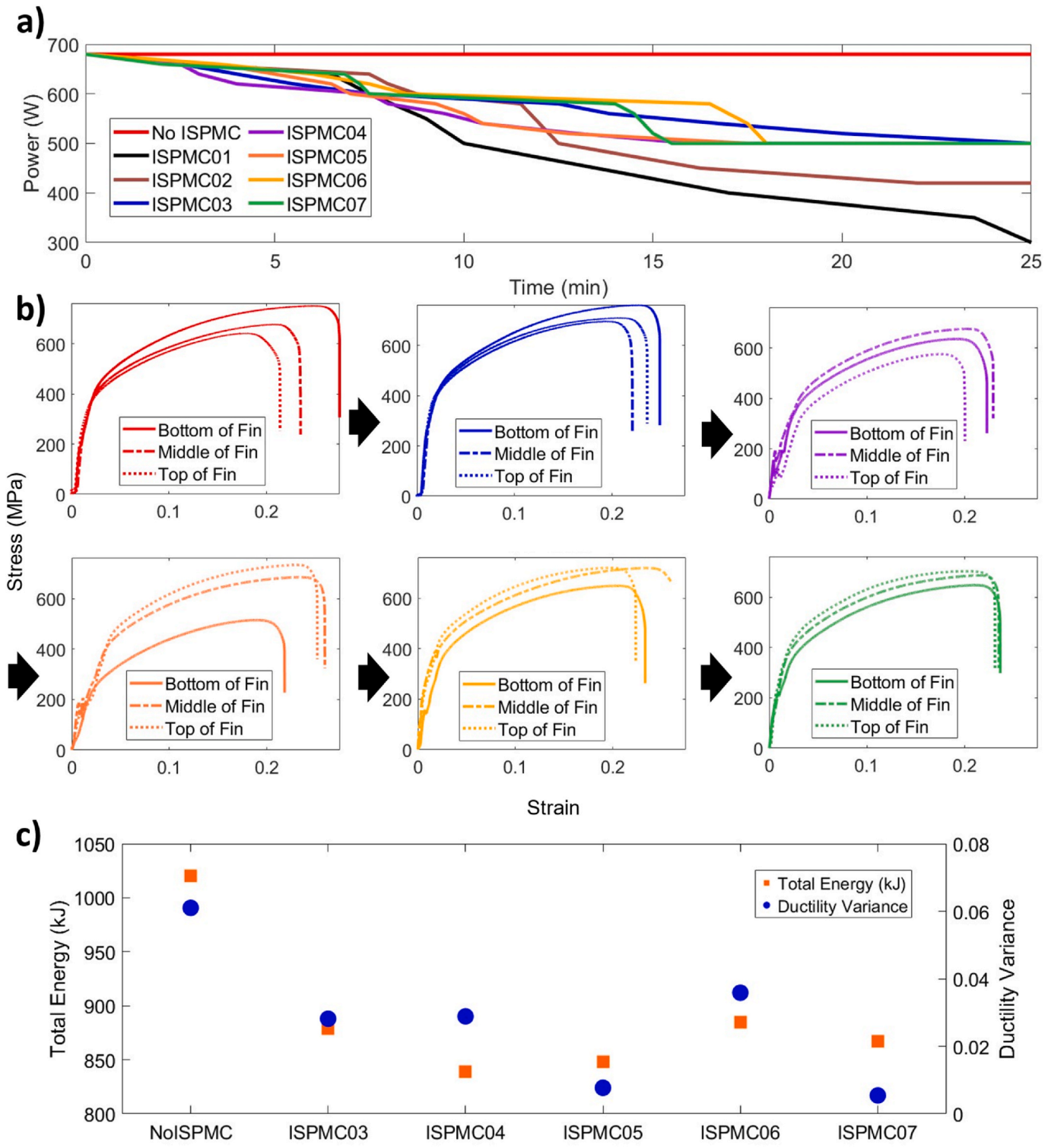

Fig. 4. ISPMC-driven real-time correction and the result on mechanical properties. **a)** Printing parameters for each generation of ISPMC that determine print quality and microstructure. **b)** Resulting engineering stress-strain for the top, middle, and bottom of a thin-walled fin for each generation of the ISPMC. **c)** Total energy vs resulting ductility variance for each generation of the ISPMC.

analysis can be seen in Fig. S2 of the SI. Overall, this behavior is consistent with the thermal profile of the build, where the upper layers cool more rapidly compared to the bottom of the build, experiencing a slower cooling. A similar analysis was performed for modulus, where the No ISPMC sample exhibited a larger difference between the top and bottom at 21.9 GPa compared to the ISPMC sample at 9.0 GPa. The two-way ANOVA indicated a statistically significant result between the sample and region, determining that the effect of location on modulus depends on the processing parameters. These results demonstrate that the No ISPMC sample results in a stronger modulus gradient between deposition layers, whereas the ISPMC sample produces a more uniform mechanical response. Since nano-indentation only provides results as reduced modulus, the data were converted using the following equation [84],

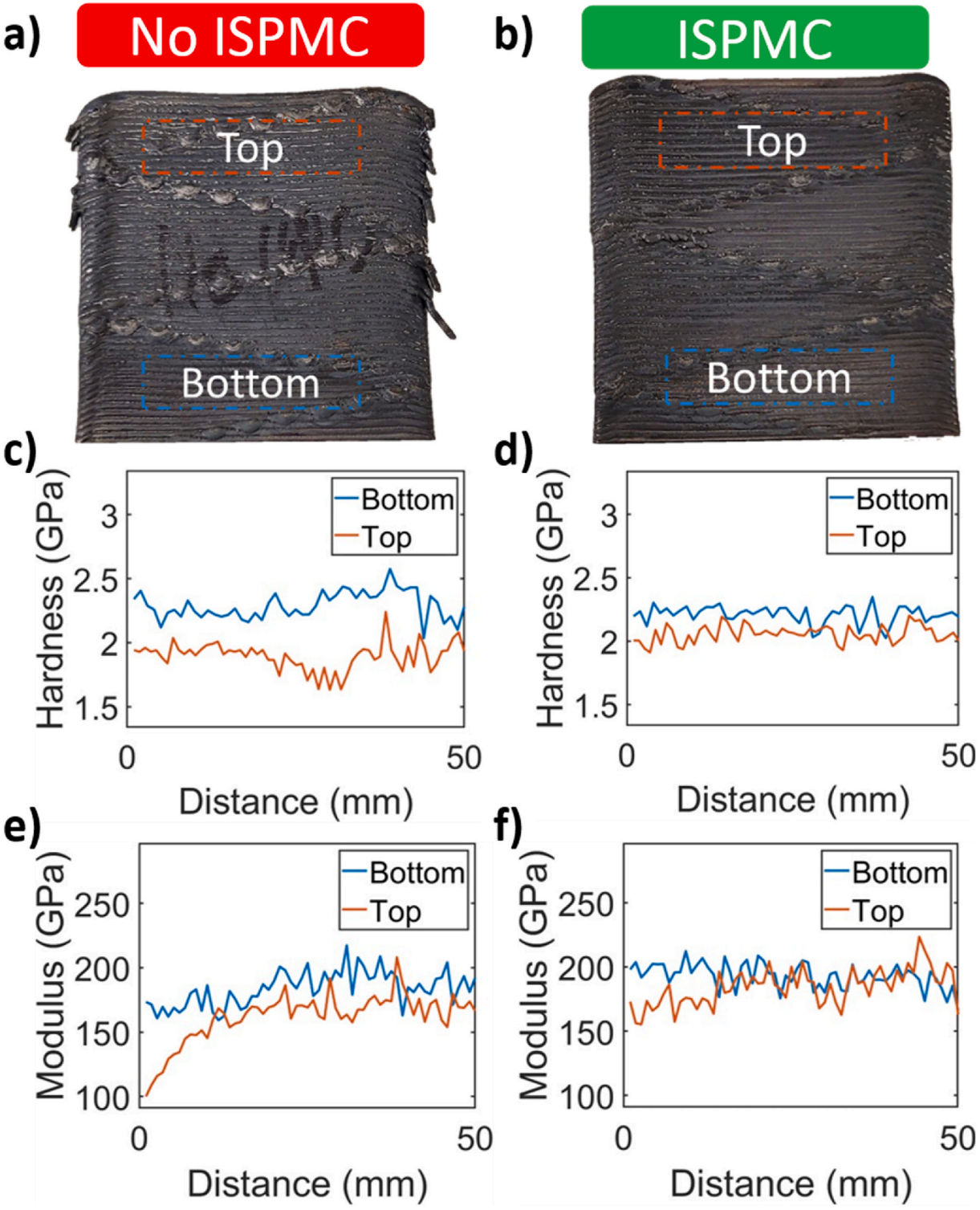

Fig. 5. Mechanical property comparison of fin prints using nano-indentation. **a)** No ISPMC fin with samples taken from top and bottom regions, and **b)** ISPMC part with samples taken from top and bottom regions, illustrate the measured locations on the fin structure. **c)** hardness of the top and bottom of the No ISPMC part plotted over the total length of the deposition. **d)** hardness of the top and bottom of the ISPMC part plotted over the length of the deposition. **e)** resulting modulus values of the No ISPMC sample. **f)** modulus values of the ISPMC part showing reduced variance in modulus from top to bottom compared to the No ISPMC part.

$$\frac{1}{E_r} = \frac{(1-\nu^2)}{E} + \frac{(1-\nu_i^2)}{E_i} \tag{1}$$

where E_r is the reduced modulus, ν is the Poisson ratio of the sample material, E is the modulus of the sample material, ν_i is the Poisson ratio of the indenter, and E_i is the modulus of the indenter. The resulting modulus for the No ISPMC sample showed in Fig. 5e, displayed a significant drop in the top region towards the edge of the sample due to the promotion of fine microstructure, leading to the lower measured modulus values. Representative optical micrographs of the electrochemically etched top and bottom regions for both the No ISPMC and ISPMC samples are provided in Fig. S4 of the SI. The No ISPMC samples

exhibited greater microstructural heterogeneity between the top and bottom regions, whereas the ISPMC sample showed a more consistent cellular grain structure throughout the build height. No significant porosity or cracking was observed in the created samples, suggesting that the observed modulus variation is more strongly associated differences in thermal history and resulting microstructural evolution across the build. In contrast, the ISPMC sample, shown in Fig. 5b, had much greater consistency in the results of both the hardness shown in Fig. 5d and modulus shown in Fig. 5f, across the part from the top of the build to the bottom of the build. This homogeneity is attributed to consistent thermal gradients and consistent solidification profiles at each region along the build, as described above. The observed trend in modulus for the No ISPMC sample, where the bottom region exhibits a higher modulus than the top region, likely reflects the difference in thermal history across deposition layers. In the absence of in-situ process monitoring and control, greater thermal gradients and reduced stabilization of melt pool behavior can produce stronger microstructural heterogeneity between layers. The bottom region experienced repeated

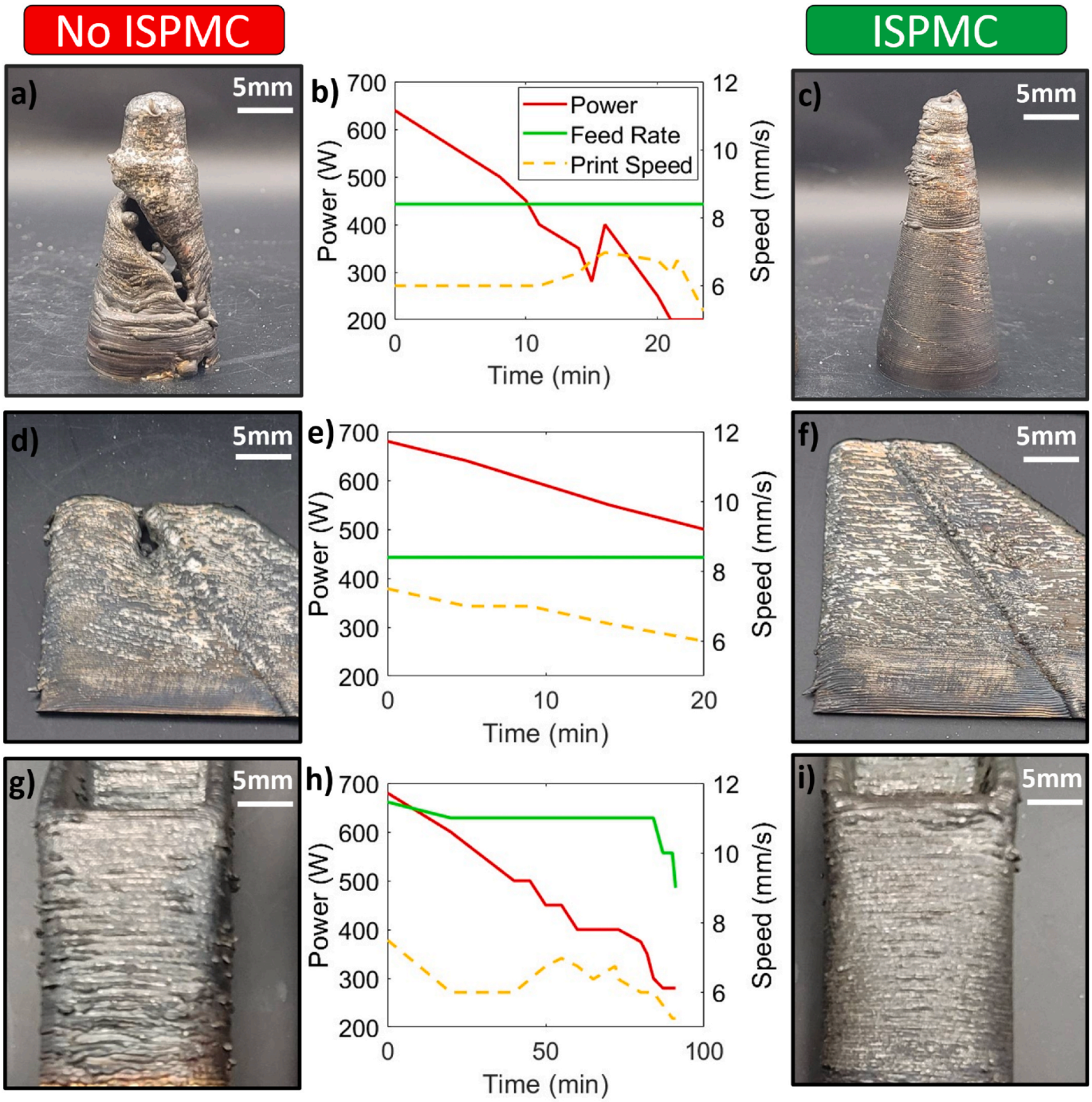

Fig. 6. In-situ process monitoring and control of component quality. **a)** Hollow cone geometry fails due to overmelting throughout the part when ISPMC was not used. **b)** Parameter plot of ISPMC cone **c)** resulting ISPMC cone with significant improvement in visual quality. **d)** Swept wing fin design fails when the process control was paused at the top of the part. **e)** Parameters plot for ISPMC swept fin **f)** resulting swept fin with full ISPMC enabled throughout print results in successful print with reduced visual defects. **g)** Circle to square transition part has significant surface roughness issues. **h)** Parameter plot of the ISPMC circle to square transition part. **i)** The resulting ISPMC circle-to-square transition part shows significant improvement in surface finish.

reheating and thermal cycling from subsequent passes, which promotes microstructural refinement and stress relaxation, resulting in a higher modulus. In contrast, the top region solidifies under different cooling conditions with less remelting, leading to a greater variation in modulus response. The reduced modulus gradient observed in the ISPMC sample suggests that active process control promotes more uniform thermal history and consequently more consistent mechanical properties across layers.

2.5. Visual, surface roughness, and geometric quality improvements using ISPMC

To demonstrate the promise of ISPMC for generating high-quality 3D printed metal components, structures with hollow regions and geometric transitions were printed. It was observed that parts printed with No ISPMC resulted in catastrophic failures, while parts with ISPMC resulted in improved part quality on the first attempt, as shown in Fig. 6. A hollow cone is a common extrusion AM geometry that faces major structural issues when printed with LDED due to the constant overhang and decreasing diameter shown in Fig. 6a. When ISPMC was implemented, overmelting was prevented by decreasing the powerlevels shown in Fig. 6b. This resulted in reduced defects in the final cone as seen in Fig. 6c. The process parameters were adjusted based on in-situ IR data, as shown in the plots in the center Fig. 6b–e and h. Interestingly, for these more complex geometries, the material feed rate and printing speed also required ISPMC-based adjustment. The plot for the parameter changes of the parts reveals a general trend in all of them that a decrease in laser power was needed; however, depending on the deposition needs, the print speeds could be increased or decreased as necessary. Another common challenging geometry for wire LDED is a swept fin. As seen in Fig. 6d, the swept fin fails with No ISPMC at the top of the print due to significant overmelting. After implementing ISPMC, the swept fin design was completed on the first attempt with significant overall quality improvements throughout the part, as shown in Fig. 6f. The final demonstration part was the circle-to-square transition, which has many aerospace and propulsion applications. Printing the circle-to-square part without ISPMC results in higher surface roughness caused by material overflow from the overmelting conditions and high print speed on the transition layers, as seen in Fig. 6g. Lowering the powerlevels and varying the print speed, as shown in Fig. 6h, resulted in an improved part. With ISPMC, the more stable melt pool resulted in a smoother surface finish across the entire geometric transition shown in Fig. 6i. Printing these geometries revealed that there was a consistent residual heat buildup from layer to layer that would cause overmelting if not corrected by ISPMC. If corrected too early, this will result in undermelting, which also leads to part failure. Additionally, some geometric transitions require a slower print speed with corresponding adjustments to feed rate and laser power. These results warrant further investigation in future studies focused on the optimization of more complex geometries.

3. Materials & methods

3.1. Meltio printing system

The LDED 3D printing approach used a wire-fed Meltio 450 system where the deposition nozzle was surrounded by 6 individual 200-W lasers for a total collective max power of 1200 W. The Meltio system was mounted to a KUKA robot arm. This printing approach allowed simple adjustment of the total laser power while printing and enabled high material feed rates. The wire used was also provided by Meltio and approved specifically for use in the Meltio 450 system. For both systems used, there were 2 sets of machine controls. The first was for the Meltio 450 head, which controls the laser power and wire feed rate. The second set of controls was for the host machine KUKA robot, which controls the print speed/movement of the Meltio Head.

3.2. Stainless steel 316L

The primary material tested was Meltio Stainless Steel 316L ER316LSI/G 19 12 3 L Si/1.4430 wire with a 1 mm diameter composed of primarily iron, with 0.02% carbon, 0.9% Silicon, 1.2 % Manganese, 18.5% chromium, 12% Nickel, 2.7% Monel [85]. SS316L was chosen because of its high availability, commonality in industry applications, and similarity to other, more advanced metals. A fin structure (50 mm width, 2 mm depth, and 50 mm height) was the primary test structure for determining microstructure and property gradients. Composed of layers 1 mm thick and 0.5 mm high, this part allowed for full IR image data of the melt pool and prior layers to be captured for the entire part from start to finish.

3.3. Infrared image capture

The LDED 3D Printing process was modified such that the hardware was best suited to fit in-situ image capture using an IR camera. IR image capture was performed using the Optris PI 08 camera manufactured by Optris GmbH & Co. KG, located in Berlin Germany where the cameras are designed, manufactured, and calibrated. This camera only captures light wavelengths outside of the laser, which are 790 nm, ensuring only melt pool data is captured. This camera was a high-quality performance grade high temperature camera with standard mounting features, allowing for the primary use of a tripod and magnetic ball and socket join mount systems for highly adjustable viewing cases. The adjustable lens's narrow depth of focus became a challenge to keep the melt pool in focus while printing 3D parts. This was addressed by mounting the camera print head, where the depth of focus now remained constant. The IR camera was set at an optimal focal distance for each print, depending on part size and the printer's range of motion. For many setups, 10-12 inches of spacing from the part was optimal. The camera shown in the SI in Fig. S3a was mounted at a 30° angle to capture the melt pool dynamics and the annealing effects on the lower layers of the print as seen in Fig. S3b. The camera's view was divided into 16 regions with respect to print location, as shown in Fig. S3c. The imaging software shown in Fig. S3d averages the IR temperature in each region and maps it on a temperature-time diagram, also creating visual heat map images. Refer to Fig. S3 in the SI for additional information.

3.4. Visual quality inspection

Microscope and visual analysis were performed, looking for and identifying voids, defects, over-melted areas, delamination between layers, and other issues to fix for improved quality, to enhance understanding and control of part microstructure. Optical Imaging Microscopy was completed with a Leica Wild M3Z Stereomicroscope.

3.5. Tensile testing

Tensile testing was conducted on samples both horizontally and vertically from the printed fins using an Instron 5982 (Instron, 825 University Ave, Norwood, MA 02062) tensile testing machine. Dog bone samples were cut from fins with surfaces post-processed to an acceptable surface finish for the tensile grips. Samples were tested randomly in batches to minimize outside influence on observations. The samples were tested at a rate of 0.1 in per minute.

3.6. Microstructure characterization

Once the parts were printed and electronic discharge-machined (wire-EDMed), several samples from them were polished and viewed under a microscope to observe porosity. These mounted samples were sanded with the Pace Nano 2000T grinder–polisher with silicon carbide paper from 180 to 1200 grit, followed by 0.05 μm alumina to achieve a mirrored polish finish. After electrochemical etching with 10 wt% oxalic

acid using a direct current of 15V for 10 s, the grain structure could be seen under a microscope. The grain structures were inspected with a Leica Wild M3Z Stereomicroscope, manufactured by Leica Microsystems' company Wild Heerbrugg, in Heerbrugg, Switzerland.

3.7. Nano-indentation

Nano-indentation was conducted with the NanoTest Vantage on the mounted and polished samples prior to etching. The nano-indentation was done using a Berkovich indenter, which is well known for its improved methods for determining hardness and reduced modulus of materials. The indenter used has a modulus of 1141 GPa and a Poisson ratio of 0.07. The diamond area function (DAF) was calibrated on fused silica to determine the manual polynomial general function to be 800d + 25.5 d^2 with the Berkovich beta factor.

4. Conclusion

This work presents a data-driven approach for in-situ process monitoring and control (ISPMC) of wire LDED printing capable of improving thermal stability, microstructural consistency, and mechanical property uniformity during fabrication. By integrating high-speed infrared thermography with computer vision-based melt pool analysis, the ISPMC system continuously monitored melt pool intensity, area, and glare to detect overmelting and undermelting conditions in real time. The framework then dynamically adjusted laser power, print speed, and feed rate to stabilize melt pool behavior and reduce thermal inconsistencies throughout the build process. The results revealed a strong relationship between thermal history, microstructure evolution, and mechanical properties in wire LDED. Uncontrolled prints experienced progressive heat accumulation and thermal cycling that produced heterogeneous grain structures and significant spatial variation in mechanical properties. Optical microscopy showed that No ISPMC samples developed mixed dendritic and cellular microstructures, while ISPMC samples maintained consistent equiaxed cellular grain structures throughout the build. These thermal and microstructural improvements translated directly into enhanced mechanical consistency. Tensile testing demonstrated up to a 90% reduction in ductility variance and a 49% reduction in ultimate tensile strength variance in ISPMC samples compared to uncontrolled prints. Nano-indentation further confirmed reduced hardness and modulus gradients between the top and bottom regions of the build, indicating improved mechanical homogeneity across deposited layers. Beyond improving microstructural and mechanical consistency, the ISPMC framework enables successful fabrication of challenging geometries including thin wall fins, hollow cones, swept fins, and circle-to-square transitions that otherwise exhibited severe defects. The ability to detect melt pool instability and implement corrective actions in real time significantly improved first-pass quality and reduced the need for trial-and-error parameter optimization. Overall, this study establishes ISPMC as a robust control strategy for wire LDED that links real time thermal monitoring with adaptive process corrections to improve print reliability and consistency. The framework provides a foundation for future intelligent metal additive manufacturing systems capable of autonomous defect mitigation, process optimization, and tailored microstructure control. The ISPMC approach has created new opportunities for rapid development of quality and microstructure control, showing immediate benefits to visual quality even on the first run of a part, which ultimately enables more complex MAM-like multi-material printing for the future. This research continues to develop systems of correction that can be tuned to achieve desired properties.

Author contributions

Conceptualization Devin J. Roach, Saegis Abbott.
Methodology Saegis Abbott, Kassandra Hernandez.
Investigation Saegis Abbott, Ryan Bertelsen, Omid Hatami Farzaneh, Doug Dingus.
Formal Analysis Saegis Abbott, Kassandra Hernandez.
Validation Saegis Abbott.
Supervision Devin J. Roach, Dong Lin.
Visualization Saegis Abbott.
Writing – Original Draft Saegis Abbott.
Writing – Review & Editing Devin J. Roach, Adam Bischoff, Ryan Bertelsen, Kassandra Hernandez, Jesse Rodriguez.
Funding Acquisition Devin J. Roach, Dong Lin.

Data availability statement

Data available on request from the authors.

Code availability

The code is available in GitHub via https://github.com/SaegisAbbott/In-Situ-Process-Monitoring-and-Control-ISPMC-with-IR-Imaging.git.

Declaration of competing interest

The authors declare that they have no known competing financial interests or personal relationships that could have appeared to influence the work reported in this paper.

Acknowledgments

D.J.R. acknowledges support from the Air Force Office of Scientific Research (AFOSR, AFRL Award No. FA8650-23-2-5202, and the Oregon State University startup funds. The authors would also like to thank the Tom & Carmen West Faculty Scholarship fund.

The authors would also like to thank Scott Campbell for assistance with tensile testing and Nick Wachenmacher for continued support and guidance of experimentation at the ATAMI facility.

Appendix A. Supplementary data

Supplementary data to this article can be found online at https://doi.org/10.1016/j.jmrt.2026.05.322.

References

[1] Revolutionary additive manufacturing : an overview - University of Johannesburg [Internet]. [cited 2025 Jul 21]. Available from: https://ujcontent.uj.ac.za/esploro/outputs/journalArticle/Revolutionary-additive-manufacturing–an-overview/9912830607691.
[2] Dilberoglu UM, Gharehpapagh B, Yaman U, Dolen M. The role of additive manufacturing in the era of industry 4.0. procedia manufacturing. 2017 Jan 1;27th international conference on flexible automation and intelligent manufacturing, FAIM2017, 27-30 June 2017, Modena, Italy11:545–554. doi:10.1016/j.promfg.2017.07.148.
[3] Fidan I, Huseynov O, Ali MA, Alkunte S, Rajeshirke M, Gupta A, et al. Recent inventions in additive manufacturing: holistic review. Inventions 2023 Aug;8(4):4. https://doi.org/10.3390/inventions8040103.
[4] Piscopo G, Iuliano L. Current research and industrial application of laser powder directed energy deposition. Int J Adv Manuf Technol 2022 Apr 1;119(11):6893–917. https://doi.org/10.1007/s00170-021-08596-w.
[5] Wilson JM, Piya C, Shin YC, Zhao F, Ramani K. Remanufacturing of turbine blades by laser direct deposition with its energy and environmental impact analysis. J Clean Prod 2014;80:170–8. https://doi.org/10.1016/j.jclepro.2014.05.084.
[6] Dadbakhsh S, Mertens R, Hao L, Van Humbeeck J, Kruth JP. Selective laser melting to manufacture "In Situ" metal matrix composites: a review. Adv Eng Mater 2019;21(3):1801244. https://doi.org/10.1002/adem.201801244.
[7] Design of in situ metal matrix composites produced by powder metallurgy—A critical review [Internet]. [cited 2025 Aug 19]. Available from: https://www.mdpi.com/2075-4701/12/12/2073.
[8] Full article: recent advance in laser powder bed fusion of Ti–6Al–4V alloys: microstructure, mechanical properties and machinability [Internet]. [cited 2025 Nov 22]. Available from: https://www.tandfonline.com/doi/full/10.1080/17452759.2024.2446952.

[9] Yeung H, Hutchinson K, Lin D. Design and implementation of laser powder bed fusion additive manufacturing testbed control. Software 2021 [Internet]. [cited 2026 Jan 5]. Available from: https://hdl.handle.net/2152/90741.
[10] Zhang X, Li D, Zheng Y, Shojaei P, Trabia M, O'Toole B, et al. In-situ synthesis of Ti5Si3-reinforced titanium matrix nanocomposite by selective laser melting: Quasi-continuous reinforcement network and enhanced mechanical performance. J Mater Process Technol 2022 Nov 1;309:117752. https://doi.org/10.1016/j.jmatprotec.2022.117752.
[11] Lin D, Richard Liu C, Cheng GJ. Single-layer graphene oxide reinforced metal matrix composites by laser sintering: microstructure and mechanical property enhancement. Acta Mater 2014 Nov 1;80:183–93. https://doi.org/10.1016/j.actamat.2014.07.038.
[12] Son K, Lee JW, Hong SJ, Pasebani S. Laser processing of an Al0. 1CoCrFeNi high entropy alloy+ Cu composite powders via laser powder bed fusion. J Powder Mater 2025;32(4):277–87.
[13] Ghanadi N, Son K, Alvarado M, Yang S, Kao HM, Chang CH, et al. Effect of LPBF processing parameters on inconel 718 lattice structures: geometrical characteristics, surface morphology, and mechanical properties. Mater Des 2025 May 1;253:113864. https://doi.org/10.1016/j.matdes.2025.113864.
[14] Irrinki H, Dexter M, Barmore B, Enneti R, Pasebani S, Badwe S, et al. Effects of powder attributes and laser powder bed fusion (L-PBF) process conditions on the densification and mechanical properties of 17-4 PH stainless steel. JOM 2016 Mar 1;68(3):860–8. https://doi.org/10.1007/s11837-015-1770-4.
[15] Hu Z, Chen F, Lin D, Nian Q, Parandoush P, Zhu X, et al. Laser additive manufacturing bulk graphene–copper nanocomposites. Nanotechnology 2017 Oct;28(44):445705. https://doi.org/10.1088/1361-6528/aa8946.
[16] Ahn SY, Jeong SG, SaGong MJ, Lee G, Kim ES, Park H, et al. Size matters: exploring part size effects on microstructure, defects, and mechanical property in optimized laser powder bed fusion (L-PBF) additive manufacturing. Mater Sci Eng A 2024 Jun 1;902:146616. https://doi.org/10.1016/j.msea.2024.146616.
[17] Khairallah SA, Martin AA, Lee JRI, Guss G, Calta NP, Hammons JA, et al. Controlling interdependent meso-nanosecond dynamics and defect generation in metal 3D printing. Science 2020 May 8;368(6491):660–5. https://doi.org/10.1126/science.aay7830.
[18] Piscopo G, Atzeni E, Saboori A, Salmi A. An overview of the process mechanisms in the laser powder directed energy deposition. Appl Sci 2023 Jan;13(1):117. https://doi.org/10.3390/app13010117.
[19] Preis J, Wang Z, Howard J, Lu Y, Wannenmacher N, Shen S, et al. Effect of laser power and deposition sequence on microstructure of GRCop42 - Inconel 625 joints fabricated using laser directed energy deposition. Mater Des 2024 May 1;241:112944. https://doi.org/10.1016/j.matdes.2024.112944.
[20] Gu D, Shi X, Poprawe R, Bourell DL, Setchi R, Zhu J. Material-structure-performance integrated laser-metal additive manufacturing. Science 2021 May 28;372(6545). https://doi.org/10.1126/science.abg1487. eabg1487.
[21] Soltani-Tehrani A, Chen P, Katsarelis C, Gradl P, Shao S, Shamsaei N. Laser powder directed energy deposition (LP-DED) NASA HR-1 alloy: laser power and heat treatment effects on microstructure and mechanical properties. Addit Manufact Lett 2022 Dec 1;3:100097. https://doi.org/10.1016/j.addlet.2022.100097.
[22] Pixner F, Buzolin R, Zelić A, Riedlsperger F, Orłowska M, Warchomicka F, et al. Tailoring the alloy composition for wire arc additive manufacturing utilizing metal-cored wires in the cold metal transfer process. Mater Des 2022 Mar 1;215:110453. https://doi.org/10.1016/j.matdes.2022.110453.
[23] Advancements in 3D printing: directed energy deposition techniques, defect analysis, and quality monitoring [Internet]. [cited 2025 Jul 21]. Available from: https://www.mdpi.com/2227-7080/12/6/86.
[24] Ghanadi N, Pasebani S. A review on wire-laser directed energy deposition: parameter control, process stability, and future research paths. J Manuf Mater Process 2024 Apr;8(2):2. https://doi.org/10.3390/jmmp8020084.
[25] Brothers E, April 11 EMGP. Aerospace Manufacturing and Design [Internet]. [cited 2025 Dec 5]. Norsk Titanium to deliver FAA-approved, 3D-printed, structural components to Boeing. Available from: https://www.aerospacemanufacturinganddesign.com/news/norsk-titanium-structural-components-boeing–041117/; 2017.
[26] Admin. DM3D Technology manufactures ten-foot-tall rocket nozzle liner for NASA project with DED 3D printing. DM3D - DED metal Addit Manufact 2021 Aug 24 [Internet]. [Internet]. [cited 2025 Dec 5]. Available from: https://dm3dtech.com/news/dm3d-technology-manufactures-ten-foot-tall-rocket-nozzle-liner-for-nasa-project-with-ded-3d-printing/.
[27] Technologies | LDED & LMJ | ADDiTEC | Metal 3D Printer Solutions. ADDiTEC [Internet]. [cited 2025 Dec 5]. Available from: https://additec3d.com/technologies/.
[28] HII installs first additively manufactured valve manifold assembly on aircraft carrier at Newport News shipbuilding. HII [Internet]. [cited 2025 Dec 5]. Available from: https://hii.com/news/hii-installs-first-additively-manufactured-valve-manifold-assembly-on-aircraft-carrier-at-newport-news-shipbuilding/.
[29] Ye L, Xue H, Li Z, Zhou Y, Chen G, Xu F, et al. Review of online quality control for laser directed energy deposition (LDED) additive manufacturing. Int J Extrem Manuf 2025. https://doi.org/10.1088/2631-7990/aded4f.
[30] Majumdar JD, Madapana D, Manna I. 3-D printing by Laser-Assisted Direct Energy Deposition (LDED): the present status. Trans Indian Natl Acad Eng 2021 Dec 1;6(4):933–53. https://doi.org/10.1007/s41403-021-00252-9.
[31] Vanaei S, Elahinia M. Applicable materials and techniques in 3D printing. In: Industrial strategies and solutions for 3D printing [Internet]. John Wiley & Sons, Ltd; 2024. p. 43–57. https://doi.org/10.1002/9781394150335.ch3 [cited 2025 Jul 21]. Available from: https://onlinelibrary.wiley.com/doi/abs/10.1002/9781394150335.ch3.
[32] Li Z, Sui S, Ma X, Tan H, Zhong C, Bi G, et al. High deposition rate powder- and wire-based laser directed energy deposition of metallic materials: a review. Int J Mach Tool Manufact 2022 Oct 1;181:103942. https://doi.org/10.1016/j.ijmachtools.2022.103942.
[33] Nagalingam AP, Shamir M, Tureyen EB, Sharman ARC, Poyraz O, Yasa E, et al. Recent progress in wire-arc and wire-laser directed energy deposition (DED) of titanium and aluminium alloys. Int J Adv Manuf Technol 2025 Jan 1;136(5):2035–73. https://doi.org/10.1007/s00170-024-14967-w.
[34] Sibisi TH, Shongwe MB, Tshabalala LC, Mathoho I. LAM additive manufacturing: a fundamental review on mechanical properties, common defects, dominant processing variables, and its applications. Int J Adv Manuf Technol 2023 Oct 1;128(7):2847–61. https://doi.org/10.1007/s00170-023-12139-w.
[35] DebRoy T, Wei HL, Zuback JS, Mukherjee T, Elmer JW, Milewski JO, et al. Additive manufacturing of metallic components – process, structure and properties. Prog Mater Sci 2018 Mar 1;92:112–224. https://doi.org/10.1016/j.pmatsci.2017.10.001.
[36] Frazier WE. Metal additive manufacturing: a review. J Mater Eng Perform 2014 Jun 1;23(6):1917–28. https://doi.org/10.1007/s11665-014-0958-z.
[37] Herzog D, Seyda V, Wycisk E, Emmelmann C. Additive manufacturing of metals. Acta Mater 2016 Sep 15;117:371–92. https://doi.org/10.1016/j.actamat.2016.07.019.
[38] Lewandowski JJ, Seifi M. Metal additive manufacturing: a review of mechanical properties. Annu Rev Mater Res 2016 Jul 1;46:151–86. https://doi.org/10.1146/annurev-matsci-070115-032024. Volume 46, 2016.
[39] Ding D, Pan Z, Cuiuri D, Li H. Wire-feed additive manufacturing of metal components: technologies, developments and future interests. Int J Adv Manuf Technol 2015 Oct 1;81(1):465–81. https://doi.org/10.1007/s00170-015-7077-3.
[40] Rose Dylan, Ranjbar Ehsan, Ghasri-Khouzani Morteza, Tavakoli Mahdi, Henein Hani, Wolfe Tonya, Qureshi Ahmed Jawad. Large-scale metal additive manufacturing: a holistic review of the state of the art and challenges - Thomas Lehmann [Internet]. [cited 2025 Nov 22]. Available from: https://journals.sagepub.com/doi/abs/10.1080/09506608.2021.1971427; 2022.
[41] Carroll BE, Palmer TA, Beese AM. Anisotropic tensile behavior of Ti–6Al–4V components fabricated with directed energy deposition additive manufacturing. Acta Mater 2015 Apr 1;87:309–20. https://doi.org/10.1016/j.actamat.2014.12.054.
[42] Yelamanchi B, Alok A, Prokop A, Martin H, Vuksanovich B, Macdonald E, et al. Influence of printing parameters on the mechanical behavior of 3D-printed SS316L parts manufactured using laser hot wire directed energy deposition. Int J Adv Manuf Technol 2024 Oct 1;134(7):3281–92. https://doi.org/10.1007/s00170-024-14308-x.
[43] Oh WJ, Lee WJ, Kim MS, Jeon JB, Shim DS. Repairing additive-manufactured 316L stainless steel using direct energy deposition. Opt Laser Technol 2019 Sep 1;117:6–17. https://doi.org/10.1016/j.optlastec.2019.04.012.
[44] Javidani M, Arreguin-Zavala J, Danovitch J, Tian Y, Brochu M. Additive manufacturing of AlSi10Mg alloy using direct energy deposition: microstructure and hardness characterization. J Therm Spray Technol 2017 Apr 1;26(4):587–97. https://doi.org/10.1007/s11666-016-0495-4.
[45] Rashkovets M, Mazzarisi M, Nikulina AA, Casalino G. Analysis of laser direct stainless steel powder deposition on Ti6Al4V substrate. Mater Lett 2020 Sep 1;274:128064. https://doi.org/10.1016/j.matlet.2020.128064.
[46] Wanni J, Achuthan A. Hetero-deformation induced (HDI) strengthening in directed energy deposited SS316L: a nanoindentation-based investigation. Mater Sci Eng A 2022 Dec 6;860:144280. https://doi.org/10.1016/j.msea.2022.144280.
[47] Elshaer RN, Elshazli AM, Hussein AHA, Al-Sayed SR. Impact of laser process parameters in direct energy deposition on microstructure, layer characteristics, and microhardness of TC21 alloy. Int J Adv Manuf Technol 2022 Aug 1;121(7):5139–54. https://doi.org/10.1007/s00170-022-09644-9.
[48] Ding RG, Huang ZW, Li HY, Mitchell I, Baxter G, Bowen P. Electron microscopy study of direct laser deposited IN718. Mater Charact 2015 Aug 1;106:324–37. https://doi.org/10.1016/j.matchar.2015.06.017.
[49] Lia F, Park JZ, Keist JS, Joshi S, Martukanitz RP. Thermal and microstructural analysis of laser-based directed energy deposition for Ti-6Al-4V and inconel 625 deposits. Mater Sci Eng, A 2018 Feb 21;717:1–10. https://doi.org/10.1016/j.msea.2018.01.060.
[50] Li Z, Chen J, Sui S, Zhong C, Lu X, Lin X. The microstructure evolution and tensile properties of inconel 718 fabricated by high-deposition-rate laser directed energy deposition. Addit Manuf 2020 Jan 1;31:100941. https://doi.org/10.1016/j.addma.2019.100941.
[51] Alam MK, Mehdi M, Urbanic RJ, Edrisy A. Electron Backscatter Diffraction (EBSD) analysis of laser-cladded AISI 420 martensitic stainless steel. Mater Charact 2020 Mar 1;161:110138. https://doi.org/10.1016/j.matchar.2020.110138.
[52] Krishna KVM, Madhavan R, Pantawane MV, Banerjee R, Dahotre NB. Machine learning based de-noising of electron back scatter patterns of various crystallographic metallic materials fabricated using laser directed energy deposition. Ultramicroscopy 2023 May 1;247:113703. https://doi.org/10.1016/j.ultramic.2023.113703.
[53] Nafar Dastgerdi J, Lotf Yasouri M, Remes H. Process-induced defects and failure mechanisms in metal additive manufacturing: a mesoscale coupled damage and plasticity modeling and X-ray computed tomography approach. Eng Fail Anal 2025 Feb 1;168:109123. https://doi.org/10.1016/j.engfailanal.2024.109123.
[54] Everton SK, Hirsch M, Stravroulakis P, Leach RK, Clare AT. Review of in-situ process monitoring and in-situ metrology for metal additive manufacturing. Mater Des 2016;95:431–45. https://doi.org/10.1016/j.matdes.2016.01.099.
[55] Assad A, Bevans BD, Potter W, Rao P, Cormier D, Deschamps F, et al. Process mapping and anomaly detection in laser wire directed energy deposition additive

manufacturing using in-situ imaging and process-aware machine learning. Mater Des 2024 Sep 1;245:113281. https://doi.org/10.1016/j.matdes.2024.113281.
[56] Ramalho A, Assad A, Bevans B, Deschamps F, Santos TG, Oliveira JP, et al. Understanding and detection of process instabilities in wire arc directed energy deposition additive manufacturing using meltpool imaging and machine learning. Mater Des 2025 Oct 1;258:114598. https://doi.org/10.1016/j.matdes.2025.114598.
[57] Gould B, Wolff S, Parab N, Zhao C, Lorenzo-Martin MC, Fezzaa K, et al. In situ analysis of laser powder bed fusion using simultaneous high-speed infrared and X-ray imaging. JOM 2021 Jan 1;73(1):201–11. https://doi.org/10.1007/s11837-020-04291-5.
[58] Chen W, Voisin T, Zhang Y, Forien JB, Spadaccini CM, McDowell DL, et al. Microscale residual stresses in additively manufactured stainless steel. Nat Commun 2019 Sep 25;10(1):4338. https://doi.org/10.1038/s41467-019-12265-8.
[59] Lough CS, Liu T, Wang X, Brown B, Landers RG, Bristow DA, et al. Local prediction of Laser Powder Bed Fusion porosity by short-wave infrared imaging thermal feature porosity probability maps. J Mater Process Technol 2022 Apr 1;302:117473. https://doi.org/10.1016/j.jmatprotec.2021.117473.
[60] Hinnebusch S, Anderson D, Bostan B, To AC. In-Situ infrared camera monitoring for defect and anomaly detection in laser powder bed fusion: calibration, data mapping, and feature extraction [Internet]. arXiv 2024. https://doi.org/10.48550/arXiv.2407.12682 [cited 2025 Aug 23]. Available from, http://arxiv.org/abs/2407.12682.
[61] Fu Y, Downey A, Yuan L, Pratt A, Balogun Y. In situ monitoring for fused filament fabrication process: a review. Addit Manuf 2021 Feb 1;38:101749. https://doi.org/10.1016/j.addma.2020.101749.
[62] Ma M, Wang Z, Wang D, Zeng X. Control of shape and performance for direct laser fabrication of precision large-scale metal parts with 316L Stainless Steel. Opt Laser Technol 2013 Feb 1;45:209–16. https://doi.org/10.1016/j.optlastec.2012.07.002.
[63] McCann R, Obeidi MA, Hughes C, McCarthy É, Egan DS, Vijayaraghavan RK, et al. In-situ sensing, process monitoring and machine control in Laser Powder Bed Fusion: a review. Addit Manuf 2021 Sep 1;45:102058. https://doi.org/10.1016/j.addma.2021.102058.
[64] Roach DJ, Rohskopf A, Hamel CM, Reinholtz WD, Bernstein R, Qi HJ, et al. Utilizing computer vision and artificial intelligence algorithms to predict and design the mechanical compression response of direct ink write 3D printed foam replacement structures. Addit Manuf 2021 May 1;41:101950. https://doi.org/10.1016/j.addma.2021.101950.
[65] Roach DJ, Rohskopf A, Leguizamon S, Appelhans L, Cook AW. Invertible neural networks for real-time control of extrusion additive manufacturing. Addit Manuf 2023 Jul 25;74:103742. https://doi.org/10.1016/j.addma.2023.103742.
[66] Hernandez KM, O'Brien S, Bischoff A, Parmigiani J, Roach DJ. Influence of 3D printing parameters on ULTEM 9085 mechanical properties using experimentation and machine learning. npj Adv Manuf 2025 Sep 16;2(1):41. https://doi.org/10.1038/s44334-025-00049-6.
[67] Gu GX, Wettermark S, Buehler MJ. Algorithm-driven design of fracture resistant composite materials realized through additive manufacturing. Addit Manuf 2017 Oct 1;17:47–54. https://doi.org/10.1016/j.addma.2017.07.002.
[68] Reu PL, Miller TJ. The application of high-speed digital image correlation. J Strain Anal Eng Des 2008 Aug 1;43(8):673–88. https://doi.org/10.1243/03093247JSA414.
[69] Landauer AK, Patel M, Henann DL, Franck C. A q-Factor-Based digital image correlation algorithm (qDIC) for resolving finite deformations with degenerate speckle patterns. Exp Mech 2018 Jun 1;58(5):815–30. https://doi.org/10.1007/s11340-018-0377-4.
[70] Wakai A, Bustillos J, Sargent N, Stokes JL, Xiong W, Smith TM, et al. Harnessing metastability for grain size control in multiprincipal element alloys during additive manufacturing. Nat Commun 2025 Feb 12;16(1):1446. https://doi.org/10.1038/s41467-025-56616-0.
[71] McBean M, Yi N, Chaplin A, Ghita O. In-process thermal monitoring of the extrusion additive manufacturing process with high temperature polymers. Virtual Phys Prototyp 2025 Sep 10;0(0):e2555497. https://doi.org/10.1080/17452759.2025.2555497.
[72] Wang R, Garcia D, Kamath RR, Dou C, Ma X, Shen B, et al. In situ melt pool measurements for laser powder bed fusion using multi sensing and correlation analysis. Sci Rep 2022 Aug 12;12(1):13716. https://doi.org/10.1038/s41598-022-18096-w.
[73] Wang R, Standfield B, Dou C, Law AC, Kong ZJ. Real-time process monitoring and closed-loop control on laser power via a customized laser powder bed fusion platform. Addit Manuf 2023 Mar 25;66:103449. https://doi.org/10.1016/j.addma.2023.103449.
[74] Critical review of LPBF metal print defects detection: roles of selective sensing technology [Internet] [cited 2025 Jul 21]. Available from: https://www.mdpi.com/2076-3417/14/15/6718.
[75] Tyralla D, Seefeld T. Thermal based process monitoring for Laser Powder Bed Fusion (LPBF). Adv Mater Res 2021;1161:123–30. https://doi.org/10.4028/www.scientific.net/AMR.1161.123.
[76] Kriczky DA, Irwin J, Reutzel EW, Michaleris P, Nassar AR, Craig J. 3D spatial reconstruction of thermal characteristics in directed energy deposition through optical thermal imaging. J Mater Process Technol 2015 Jul 1;221:172–86. https://doi.org/10.1016/j.jmatprotec.2015.02.021.
[77] Marshall GJ, Young WJ, Thompson SM, Shamsaei N, Daniewicz SR, Shao S. Understanding the microstructure formation of Ti-6Al-4V during direct laser deposition via In-Situ thermal monitoring. JOM 2016 Mar 1;68(3):778–90. https://doi.org/10.1007/s11837-015-1767-z.
[78] Ya W, Konuk AR, Aarts R, Pathiraj B. Huis in 't Veld B. Spectroscopic monitoring of metallic bonding in laser metal deposition. J Mater Process Technol 2015 Jun 1;220:276–84. https://doi.org/10.1016/j.jmatprotec.2015.01.026.
[79] Herzog T, Brandt M, Trinchi A, Sola A, Hagenlocher C, Molotnikov A. Defect detection by multi-axis infrared process monitoring of laser beam directed energy deposition. Sci Rep 2024 Feb 16;14(1):3861. https://doi.org/10.1038/s41598-024-53931-2.
[80] Wei J, He Y, Wang F, He Y, Rong X, Chen M, et al. Convolutional neural network assisted infrared imaging technology: an enhanced online processing state monitoring method for laser powder bed fusion. Infrared Phys Technol 2023 Jun 1;131:104661. https://doi.org/10.1016/j.infrared.2023.104661.
[81] Meng W, Chen K, Pan Q, Ye K, Liu Z, Ma Q, et al. Narrow gap welding of 316L thick-section steel with cold metal transition pulsed arc swing. Int J Adv Manuf Technol 2024 Jun 1;132(7):4035–53. https://doi.org/10.1007/s00170-024-13601-z.
[82] Liu S, Lee M, Choi C, Shin K. Effect of additive manufacturing of SUS316L using selective laser melting. J Mater Res Technol 2023 May 1;24:9824–33. https://doi.org/10.1016/j.jmrt.2023.05.160.
[83] Jeyaprakash N, Saravana Kumar M, Yang CH, Cheng Y, Radhika N, Sivasankaran S. Effect of microstructural evolution during melt pool formation on nano-mechanical properties in LPBF based SS316L parts. J Alloys Compd 2024 Jan 25;972:172745. https://doi.org/10.1016/j.jallcom.2023.172745.
[84] Oliver WC, Pharr GM. An improved technique for determining hardness and elastic modulus using load and displacement sensing indentation experiments. J Mater Res 1992 Jun 1;7(6):1564–83. https://doi.org/10.1557/JMR.1992.1564.
[85] Meltio_Stainless_Steel_316L_datasheet_v8_04-12-2025 [Internet]. Available from: https://meltio3d.com/wp-content/uploads/2026/01/Meltio_Stainless_Steel_316L_datasheet_v8_04-12-2025.pdf.